ACS Sustainable Chemistry & Engineering

Research Article

pubs.acs.org/journal/ascecg

Preparation and Electrochemical Characterization of Hollow Hexagonal $NiCo_2S_4$ Nanoplates as Pseudocapacitor Materials

Jun Pu,[†] Fangling Cui,[†] Sibin Chu,[†] Tingting Wang,[‡] Enhong Sheng,[†] and Zhenghua Wang*,[†]

[†]Key Laboratory of Functional Molecular Solids, Ministry of Education, College of Chemistry and Materials Science, Anhui Normal University, Wuhu 241000, P. R. China

[‡]School of Chemical Engineering, Wuhan University of Technology, Wuhan, 430070, P. R. China

ABSTRACT: In this study, the binary transition metal sulfide $NiCo_2S_4$ with a novel hollow hexagonal nanoplate (HHNs) structure has been synthesized through a sacrificial template method based on the Kirkendall effect. The hollow nanoplates have an average diameter of about 200 nm, thickness of about 50 nm, and shell thickness of about 10 nm. The resulting samples were characterized by means of XRD, XPS, EDX, SEM, TEM, and HRTEM. The electrochemical characterization results demonstrate that $NiCo_2S_4$ hollow hexagonal nanoplates exhibit a high specific capacitance of 437 F g^{-1} in a 3 M KOH aqueous electrolyte at a current rate of 1 A g^{-1}, along with a superior rate capability and Coulombic efficiency stability, indicating their potential application as electrode materials for supercapacitors.

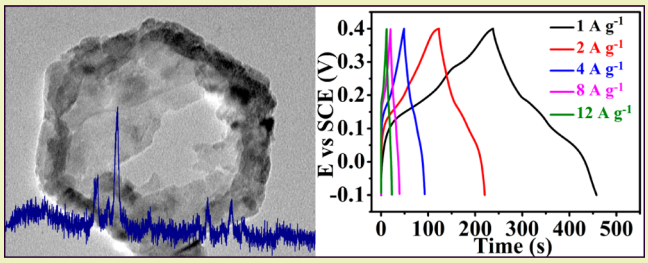

KEYWORDS: *Hollow hexagonal nanoplates, $NiCo_2S_4$, Supercapacitors, Kirkendall effect*

INTRODUCTION

It is well known that rechargeable supercapacitors have received intense interest and have wide applications in portable electronic devices, uninterruptible power supplies, hybrid electrical vehicle systems, and renewable energies due to their high power density, long cycle life, low cost, and rapid charge−discharge processes, compared to lithium-ion batteries and traditional capacitors.[1−7]

The electrode material is the key factor that determines the performance of supercapacitors. In general, supercpacitors can be divided into two types, electrochemical double-layer capacitors (EDLCs) and redox pseudocapacitors, depending upon the available electrochemical mechanisms of energy storage.[8−10] For EDLCs that are based on carbon materials, the electrical charge is a physical charge separation that is stored at the interfaces between the electrodes and electrolytes.[11] By contrast, the Faradic pseudocapacitors that are based on metal oxides, hydroxide,s and conductive polymers come from reversible redox reactions within the active materials.[12−14] The carbon materials as working electrodes have many advantages, such as excellent stability and low cost. However, they usually suffer from a low capacitance of 100−200 F g^{-1}.[15−17] The specific capacitance and energy density of pseudocapacitors associated with Faradaic reactions are substantially higher than those of EDLCs.[18,19] Therefore, the development of pseudocapacitor electrode materials becomes a new research hotspot.

Metal sulfides with unique photochemical and electrochemical characteristics have many potential applications in areas of optics, catalysis, sensing, solar energy, and batteries.[20−22] To date, a series of metal sulfides have been prepared through different methods, such as NiS,[23] MnS,[24] ZnS,[25] CdS,[26] CuS,[27] and CoS_2.[28] In recent years, more and more attention has been paid to the application of metal sulfides in pseudocapacitors. For instance, Zheng et al. reported the electrochemical performance of flower-like β-NiS.[29] Rao et al. prepared sphere-like CoS nanostructures that showed a high specific capacitance of 354 F g^{-1} at 0.5 A g^{-1}.[30] Lou et al. obtained CoS_2 tube-like cavities by a moderate solvothermal method and revealed a high capacitance.[31] Although many transition metal sulfides have been investigated as supercapacitor electrode materials, reports on binary transition metal sulfides as supercapacitor electrode materials is still limited. In recent studies by Jiang et al., $NiCo_2S_4$ porous nanotubes and urchin-like nanostructures were applied as pseudocapacitor electrode materials and showed good electrochemical activities.[32,33]

The Kirkendall effect was first studied by Kirkenddall and Smigelskas in 1947.[34] It is basically based on the mutual diffusion process through an interface of two metals so that vacancy diffusion occurs to compensate for the unequality of the material flow and that the initial interface moves.[35,36] Recently, various hollow nanostructures have been synthesized on the basis of the Kirkendall effect. For example, Alivisatos et al. successfully fabricated hollow cobalt sulfide nanospheres.[37] Fan and coworkers reported the preparation of $ZnAl_2O_4$ spinel nanotubes through an interfacial reaction of $ZnO-Al_2O_3$ nanowires involving the Kirkendall effect.[38] Sun et al. prepared CeO_2 nanotubes from $Ce(OH)CO_3$ nanorods through Kirkendall diffusion.[39]

Received: November 13, 2013
Revised: November 28, 2013
Published: December 23, 2013

In this work, we demonstrated a methodology toward the preparation of $NiCo_2S_4$ with a novel nanostructure of hollow hexagonal nanoplates (HHNs) on the basis of the Kirkendall effect. Additionally, the as-prepared $NiCo_2S_4$ HHNs revealed a high specific capacitance of 437 F g^{-1} at 1 A g^{-1}, which showed potential applications as supercapacitor electrode materials.

EXPERIMENTAL SECTION

Materials. Reagents cobalt chloride hexahydrate ($CoCl_2{\cdot}6H_2O$), nickel acetate tetrahydrate ($Ni(Ac)_2{\cdot}4H_2O$), sodium sulfide (Na_2S), sodium hydroxide (NaOH), potassium hydroide (KOH), and absolute ethanol were commercially available from Sinopharm Chemical Reagent Co. in analytical grade and were used without further purification. Deionized water with an electrical resistance of 18 MΩ is used throughout.

Synthesis of Precursor Serving as the Templates. In a typical experiment, 0.476 g of $CoCl_2{\cdot}6H_2O$ (4 mmol) and 0.249 g of $Ni(Ac)_2{\cdot}4H_2O$ (2 mmol) were dissolved in 40 mL of deionized water to obtain a light pink solution, and then 3.2 g of NaOH was added. After stirring for 10 min, the solution was transferred into a Teflon-lined stainless-steel autoclave and heated at 160 °C for 20 h. After cooling to room temperature naturally, the gray precipitate was collected and washed with deionized water several times and then dried at 60 °C for 5 h.

Template-Directed Synthesis of $NiCo_2S_4$ HHNs. First, 0.093 g of the as-obtained precursor was dispersed into 30 mL of deionized water through ultrasonication. Then, 5 mL of 0.5 M Na_2S solution was added into the above suspension. After stirring for 5 min, the suspension was transferred into a 40 mL Teflon-lined stainless-steel autoclave. The autoclave was heated at 160 °C for 12 h and then cooled to room temperature naturally. The as-obtained black precipitate was collected by filtration and washed with deionized water and ethanol for several times each to remove the possible impurities. The resulting final product was dried in vacuum at 50 °C for 2 h. The panoramic schematic route is depicted in Figure 1.

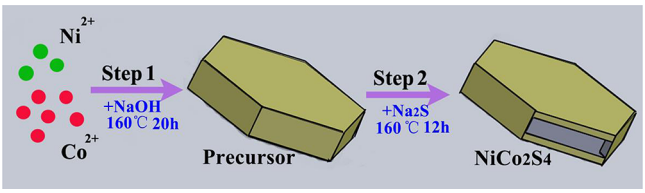

Figure 1. Schematic illustration of the formation process of the hollow $NiCo_2S_4$ hexagonal nanoplates using a two-step route.

Characterizations. X-ray diffraction (XRD) patterns were obtained on a Rigaku D/MAX2500 V with Cu Kα radiation (λ = 1.5418 Å). Scanning electron microscopy (SEM) images and energy dispersive X-ray spectrometer (EDX) were taken with a Hitachi S-4800 scanning electron microscope. X-ray photoelectron spectroscopies (XPS) were recorded on an ESCALab MKII X-ray photoelectron spectrometer with nonmonochromatized Mg Kα X-ray as the excitation source. The binding energies in XPS analysis were corrected by referencing C 1s to 284.6 eV. Transmission electron microscopy (TEM) and high-resolution transmission electron microscopy (HRTEM) images were recorded on a FEI Tecnai G^2 20 high-resolution transmission electron microscope performed at an acceleration voltage of 200 kV.

Electrochemical Measurements. The working electrodes were prepared by pressing a mixture of the as-prepared $NiCo_2S_4$ sample, acetylene black, and polytetrafluoroethylene (PTFE) binder with a weight ratio of 85:10:5 onto a nickel foam current collector and dried at 50 °C for 6 h. Each electrode contained about 2.4 mg of electroactive material and had a geometric surface area of about 1 cm^2. A platinum wire and standard calomel electrode (SCE) were used as the counter and reference electrodes in a 3 M KOH solution, respectively. Electrochemical experiments were performed on a CHI660D electrochemical analyzer (ChenHua Corp., Shanghai, China) with a three-electrode experimental setup.

RESULTS AND DISCUSSIONS

The composition of the precursor and $NiCo_2S_4$ samples were determined by XRD. Figure 2a shows a typical XRD pattern of

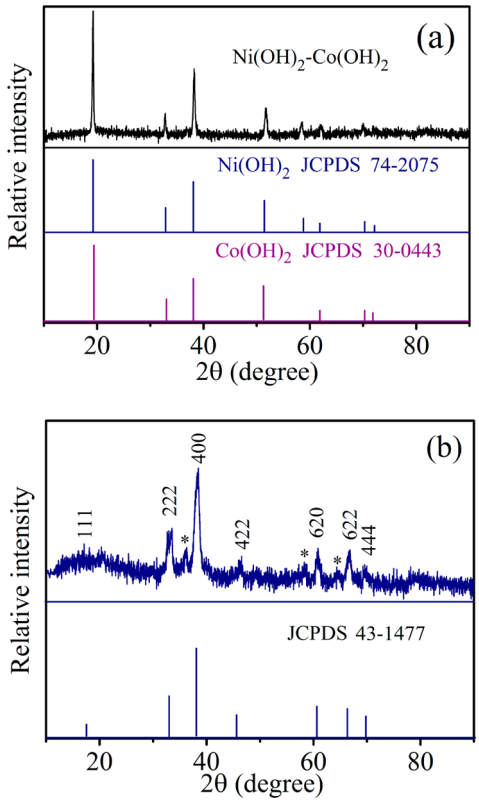

Figure 2. XRD patterns of the (a) precursor sample and (b) $NiCo_2S_4$ sample.

the precursor, the diffraction peaks of which correspond to both $Ni(OH)_2$ (JCPDS No. 74-2075) and $Co(OH)_2$ (JCPDS No. 30-0443). As $Ni(OH)_2$ and $Co(OH)_2$ have similar structures and very close diffraction peaks, it is difficult to differentiate these two phases from XRD. Figure 2b displays a typical XRD pattern of the $NiCo_2S_4$ sample prepared by hydrothermally treating the precursor with Na_2S solution, which corresponds to spinel $NiCo_2S_4$ (JCPDS No. 43-1477). Several weak diffraction peaks that are marked with asterisks can be ascribed to Ni_3S_4 (JCPDS No. 43-1469).

X-ray photoelectron spectroscopy (XPS) analysis is an effective technique to investigate the surface elemental composition. Figure 3a shows a survey XPS spectrum of the $NiCo_2S_4$ sample in the range of 0−1300 eV. The peaks at 162.7, 779.9, and 855.7 eV correspond to S 2p, Co 2p, and Ni 2p, respectively, indicating the existence of S, Co, and Ni elements in the $NiCo_2S_4$ sample. The C (as reference) and O elements are due to exposure to the air. The Co 2p and Ni 2p spectra were computer fitted using a Gaussian fitting method considering two spin−orbit doublets and two shakeup satellites. As depicted in Figure 3b, the energy difference between Ni $2p_{3/2}$ (855.6 eV) and Ni $2p_{1/2}$ (873.4 eV) is 17.8 eV indicate the existence of both Ni^{2+} and Ni^{3+}.[40] The strong peaks at 779.2 eV for Co $2p_{3/2}$ and 796.5 eV for Co $2p_{1/2}$ are demonstrated in Figure 3c, indicating both Co^{3+} and Co^{2+} in the $NiCo_2S_4$ sample.[33] Figure 3d shows the

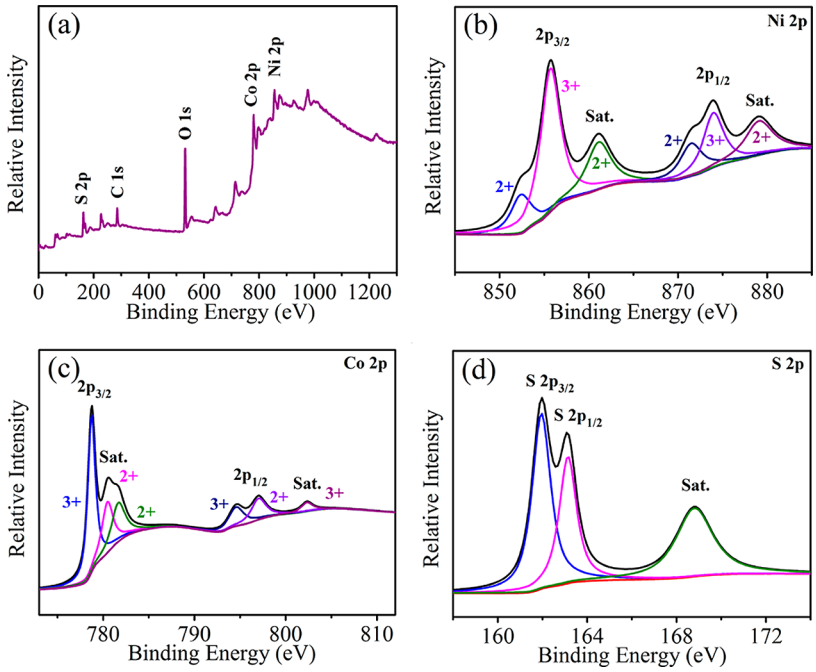

Figure 3. XPS spectra of the as-obtained $NiCo_2S_4$ sample: (a) survey, (b) Ni 2p, (c) Co 2p, and (d) S 2p.

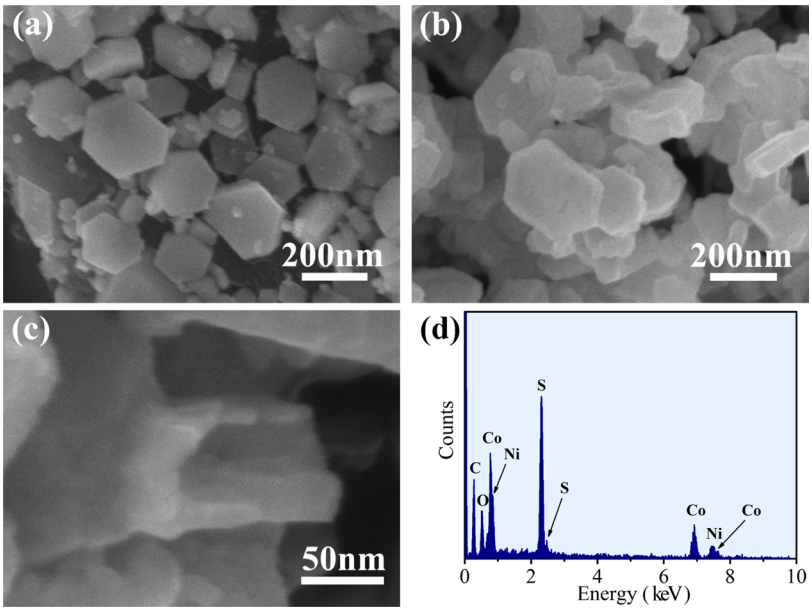

Figure 4. SEM images of the (a) precursor, (b,c) $NiCo_2S_4$ HHNs with different magnification, and (d) EDX spectrum of the $NiCo_2S_4$ HHNs.

core level spectrum of the S 2p region, and the binding energies at 163.1 and 161.8 eV correspond to S $2p_{1/2}$ and S $2p_{3/2}$, respectively.[41]

The genuine shape and size of the precursor and $NiCo_2S_4$ samples were investigated using the SEM technique. Figure 4a shows a typical SEM image of the precursor sample, in which many uniform hexagonal nanoplates with an average diameter of about 200 nm and thickness of about 50 nm are shown. Figure 4b displays a SEM image of the $NiCo_2S_4$ sample prepared by treating the precursor in Na_2S solution at 160 °C for 12 h. The as-obtained $NiCo_2S_4$ sample still retains the hexagonal nanoplate morphology of the precursor. Specifically, a broken nanoplate (Figure 4c) clearly reveals the hollow structure of the $NiCo_2S_4$ HHNs. The shell thickness of the $NiCo_2S_4$ HHNs estimated from this figure is about 10 nm. Energy dispersive X-ray (EDX) analysis in Figure 4d further proves the existence of Co, Ni, and S elements in the $NiCo_2S_4$ HHNs. The atom ratio of Ni, Co, and S is 1:1.76:3.93, which agrees well with the theoretical value of $NiCo_2S_4$.

TEM and HRTEM are applied to further analyze the morphology of the as-obtained samples. The TEM image of the Ni−Co hydroxide precursor in Figure 5a displays a solid hexagonal nanosheet, which is similar to the SEM result in Figure 3a. Figure 5b and c are the TEM images of the $NiCo_2S_4$ sample with different magnifications, which further demonstrated the hollow structure of the nanosheets. The shell thickness of the hollow nanosheets is about 10 nm. As the $NiCo_2S_4$ HHNs still retain the hexagonal sheet-like structure of the precursor, it is

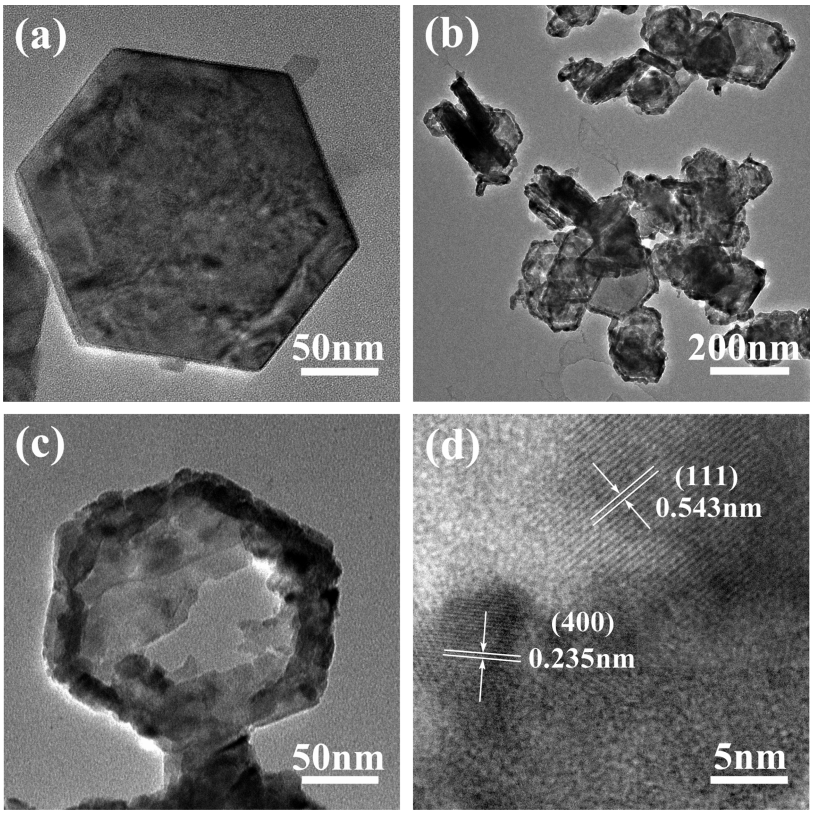

Figure 5. (a) TEM image of the precursor sample. (b,c) TEM images of $NiCo_2S_4$ HHNs. (d) HRTEM image of $NiCo_2S_4$ HHNs.

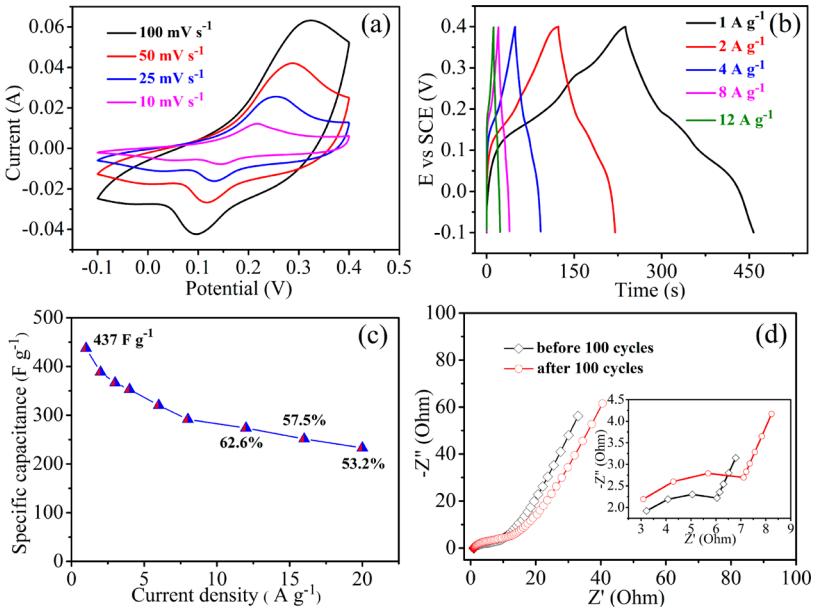

Figure 6. (a) CV curves of the $NiCo_2S_4$ sample measured at different scan rates. (b) Galvanostatic charge−discharge profiles of the $NiCo_2S_4$ sample at current density in the range of 1−12 A g^{-1}. (c) Specific capacitances of the $NiCo_2S_4$ sample at various current densities. (d) Nyquist plots of sample before and after 100 cycles charge/discharge processes. Inset is the Nyquist plots fitted by Zview software.

reasonable to conclude that the precursor serves as a sacrificial template for the growth of $NiCo_2S_4$ HHNs. The HRTEM image of $NiCo_2S_4$ HHNs is displayed in Figure 5d. The observed interplanar spacing is measured to be 0.235 and 0.543 nm, which matches well with the (400) and (111) lattice planes of spinel $NiCo_2S_4$.[33] The hollow structure increases the surface-to-bulk ratio and thus increases the contact area between the active material and the electrolyte, leading to more efficient ion and electron transportation, which may result in improved electrochemical performances when acting as supercapacitor electrode materials.[42,43]

The formation of the $NiCo_2S_4$ hollow nanosheets can be illustrated by the Kirkendall effect. At the earlier stage of the hydrothermal reacting process, the reaction between S^{2-} ions

and $Ni(OH)_2$−$Co(OH)_2$ nanoplates result in the production of a thin layer of $NiCo_2S_4$ nanoparticles on the surface of the nanoplates. As proposed by Yin et al.,[44] the direct conversion of the precursor core to the $NiCo_2S_4$ shell is therefore obstructed by the layer, so further reaction will continue by the diffusion of S^{2-} ions through the interface. Because the outward diffusion rate of the cobalt source is faster than the inward transport rate of S^{2-} ions through the $NiCo_2S_4$ shell, the unequal diffusion of reacting species will produce voids close to the interface.[35] With the reaction continuing, the $NiCo_2S_4$ shell is increased, and the precursor core is decreased gradually. Finally, $NiCo_2S_4$ hollow nanostructures are obtained.

The electrochemical properties of $NiCo_2S_4$ HHNs are investigated by cyclic voltammetry (CV), galvanostatic charge−discharge, and electrical impedance measurements in 3 M KOH as the electrolyte at ambient temperature. Figure 6a presents the CV curves of the $NiCo_2S_4$ sample in the potential window of −0.2 to 0.4 V at different scan rates of 10, 25, 50, and 100 mV s^{-1}. According to these curves, there is an integrated oxidation peak and two reduction peaks. The height of peak currents varies, and a progressive shift of the peaks to a higher potential is observed, confirming the pseudocapacitive behavior of the $NiCo_2S_4$ hollow nanoplates. The mechanism of electrochemical reactions may be explained by the diffusion of OH^- ions. At low scan rates, the movement of OH^- ions is slower than that at high scan rates, and the utilization ratio of electrode material is higher, which promotes rich redox reactions of $NiCo_2S_4$ samples during the cycling process.[33,45] The broad redox reaction peaks may come from the reversible Faradaic redox processes of $Co^{2+}/Co^{3+}/Co^{4+}$ and Ni^{2+}/Ni^{3+} in KOH solution[32]

$$CoS + OH^- \rightleftarrows CoSOH + e^-$$

$$CoSOH + OH^- \rightleftarrows CoSO + H_2O + 2e^-$$

$$NiS + OH^- \rightleftarrows NiSOH + e^-$$

Figure 6b shows the charge−discharge curves of the as-prepared samples at different current densities. Clearly, the curves at low current densities show two platforms, corresponding to the redox reactions. Also, with current density increases, the discharge time reduces. The specific capacitances calculated from these discharge curves are according to the following equation[11]

$$C = \frac{I \times \Delta t}{m \times \Delta V}$$

where C (F g^{-1}) is the specific capacitance of the electrode based on the mass of active materials, I (A) is the current during discharge process, Δt (s) is the discharge time, ΔV (V) is the potential window (in present work, $\Delta V = 0.5$ V), and m (g) is the mass of active materials ($NiCo_2S_4$). In addition, specific capacitances (C) of the $NiCo_2S_4$ samples at various current densities from 1 to 20 A g^{-1} are plotted in Figure 6c. In detail, the samples take on the best specific capacitance of 437 F g^{-1} at 1 A g^{-1}. Along with an increase in current densities, the corresponding specific capacitances gradually decrease. Notably, the $NiCo_2S_4$ sample show a high capacitance retention of about 53.2% at a high current density of 20 A g^{-1}, suggesting its good rate capability.

Figure 6d displays the Nyquist plots of $NiCo_2S_4$ before and after 100 cycles in the frequency range of 100 kHz to 0.01 Hz, as well as the Nyquist plots fitted by Zview software (inset in Figure 6d). In the Nyquist plots, semicircles are observed in the high-frequency region, which affiliates with the electrolyte resistance.[46] The linear part after the semicircle involves the diffusion process of ions. The slopes of about 50° (before cycling) and 45° (after cycling) of the Nyquist plot demonstrates the fast ion transfer between electrode and electrolyte.[47,48] From the comparison of these two impedance curves, the semicircular arc of $NiCo_2S_4$ samples after 100 charge−discharge cycles has increased in size, which can be ascribed to the enhancement of the charge−transfer resistance in the electrode reaction.[49] Furthermore, on the basis of the proposed equivalent circuit model by the fitting of Zview software, the overall resistance (R_t) consisting of electrical connection resistance (R_e), electrolyte resistance (R_s), and resistance of ion migration in samples micropores (R_p) are calculated and listed in Table 1.

Table 1. Overall Resistance (R_t), Electrical Connection Resistance (R_e), Electrolyte Resistance (R_s), and Resistance of Ion Migration in Micropores (R_p) of the Samples

	resistance (ohm)			
samples	R_t	R_s	R_e	R_p
before cycling	6.796	3.216	2.302	1.278
after 100 cycles	8.231	3.086	2.790	2.355

To evaluate the cycling stability of the $NiCo_2S_4$ HHNs electrode, the values of specific capacitance with respect to charge−discharge cycle number (up to 1000 cycles) at a current density of 2 A g^{-1} are measured, as shown in Figure 7. The specific capacitances of $NiCo_2S_4$ electrode decrease from 388 to 314 F g^{-1} after 1000 cycles, with a retention of 81% of the initial value, higher than the previously reported $NiCo_2S_4$ nanotubes (63% retention).[32] It is important that the capacitance tends to stable after about 700 cycles and the Coulombic efficiency almost remained 100%. The good cycle stability indicates a superior reversible surface reaction between the electrode and electrolyte, which might find possible applications as an electrode material in supercapacitors.

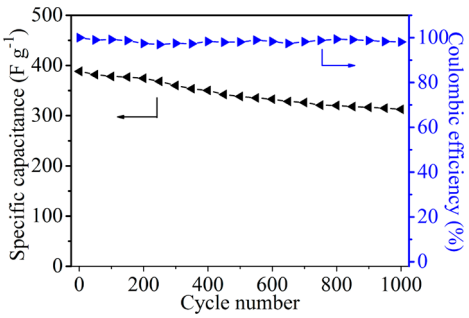

Figure 7. Specific capacitance and Coulombic efficiency vs cycle number at a current density of 2 A g^{-1}.

CONCLUSIONS

In summary, $NiCo_2S_4$ hollow hexagonal nanoplates are successfully prepared through a hydrothermal route by using Ni−Co double hydroxide precursor nanoplates as sacrificial templates based on the Kirkendall effect. The hollow nanostructure provides a relatively short diffusion pathway for ions when acting as supercapacitor electrode materials, leading to high utilization of active materials. The as-obtained $NiCo_2S_4$ samples show a high specific capacitance of 437 F g^{-1} at a current

density of 1 A g^{-1}, which ensure them as promising electrode materials for practical applications.

AUTHOR INFORMATION

Corresponding Author

*Tel.: +86-553-3869303. Fax: +86-553-3869302. E-mail: zhwang@mail.ahnu.edu.cn.

Notes

The authors declare no competing financial interest.

ACKNOWLEDGMENTS

Financial support from the National Natural Science Foundation of China (Project No. 21171006) is gratefully acknowledged.

REFERENCES

(1) Boukhalfa, S.; Evanoff, K.; Yushin, G. Atomic layer deposition of vanadium oxide on carbon nanotubes for high-power supercapacitor electrodes. *Energy Environ. Sci.* **2012**, *5*, 6872−6879.

(2) Sun, X. F.; Xu, Y. L.; Wang, J.; Mao, S. C. The composite film of polypyrrole and functionalized multi walled carbon nanotubes as an electrode material for supercapacitors. *Int. J. Electrochem. Sci.* **2012**, *7*, 3205−3214.

(3) Liu, D. Q.; Wang, Q.; Qiao, L.; Li, F.; Wang, D. S.; Yang, Z. B.; He, D. Y. Preparation of nano-networks of MnO_2 shell/Ni current collector core for high-performance supercapacitor electrodes. *J. Mater. Chem.* **2012**, *22*, 483−487.

(4) Ye, S. B.; Feng, J. C.; Wu, P. Y. Deposition of three-dimensional graphene aerogel on nickel foam as a binder-free supercapacitor electrode. *ACS Appl. Mater. Interfaces* **2013**, *5*, 7122−7129.

(5) Jiang, H.; Li, C. Z.; Sun, T.; Ma, J. A green and high energy density asymmetric supercapacitor based on ultrathin MnO_2 nanostructures and functional mesoporous carbon nanotube electrodes. *Nanoscale* **2012**, *4*, 807−812.

(6) Wei, D.; Scherer, M. R. J.; Bower, C.; Andrew, P.; Ryhänen, T.; Steiner, U. A nanostructured electrochromic supercapacitor. *Nano Lett.* **2012**, *12*, 1857−1862.

(7) Zhang, X. J.; Shi, W. H.; Zhu, J. X.; Kharistal, D. J.; Zhao, W. Y.; Lalia, B. S.; Hng, H. H.; Yan, Q. Y. High-power and high-energy-density flexible pseudocapacitor electrodes made from porous CuO nanobelts and single-walled carbon nanotubes. *ACS Nano* **2011**, *3*, 2013−2019.

(8) Jiang, R. R.; Huang, T.; Liu, J. L.; Zhuang, J. H.; Yu, A. S. A novel method to prepare nanostructured manganese dioxide and its electrochemical properties as a supercapacitor electrode. *Electrochim. Acta* **2009**, *54*, 3047−3052.

(9) Zhang, H. H.; Wang, Y. Q.; Liu, C. W.; Jiang, H. T. Influence of surfactant CTAB on the electrochemical performance of manganese dioxide used as supercapacitor electrode material. *J. Alloys Compd.* **2012**, *517*, 1−8.

(10) Xie, L. J.; Li, K. X.; Sun, G. H.; Hu, Z. G.; Lv, C. X.; Wang, J. L.; Zhang, C. M. Preparation and electrochemical performance of the layered cobalt oxide (Co_3O_4) as supercapacitor electrode material. *J. Solid State Electrochem.* **2013**, *17*, 55−61.

(11) Gao, Z.; Wang, J.; Li, Z. S.; Yang, W. L.; Wang, B.; Hou, M. J.; He, Y.; Liu, Q.; Mann, T.; Yang, P. P.; Zhang, M. L.; Liu, L. H. Graphene nanosheet/Ni^{2+}/Al^{3+} layered double-hydroxide composite as a novel electrode for a supercapacitor. *Chem. Mater.* **2011**, *23*, 3509−3516.

(12) Du, W.; Liu, R. M.; Jiang, Y. W.; Lu, Q. Y.; Fan, Y. Z.; Gao, F. Facile synthesis of hollow Co_3O_4 boxes for high capacity supercapacitor. *J. Power Sources* **2013**, *227*, 101−105.

(13) Li, Y. Z.; Zhao, X.; Yu, P. P.; Zhang, Q. H. Oriented arrays of polyaniline nanorods grown on graphite nanosheets for an electrochemical supercapacitor. *Langmuir* **2013**, *29*, 493−500.

(14) Ji, X. B.; Hallam, P. M.; Houssein, S. M.; Kadara, R.; Lang, L. M.; Banks, C. E. Printable thin film supercapacitors utilizing single crystal cobalt hydroxide nanosheets. *RSC Adv.* **2012**, *2*, 1508−1515.

(15) Kaempgen, M.; Chan, C. K.; Ma, J.; Cui, Y.; Gruner, G. Printable thin film supercapacitors using single-walled carbon nanotubes. *Nano Lett.* **2009**, *9*, 1872−1876.

(16) Huang, C.; Grobert, N.; Watt, A. A. R.; Johnston, C.; Crossley, A.; Young, N. P.; Grant, P. S. Layer-by-layer spray deposition and unzipping of single-wall carbon nanotube-based thin film electrodes for electrochemical capacitors. *Carbon* **2013**, *61*, 525−536.

(17) Jang, Y. S.; Jo, J. D.; Choi, Y. M.; Kim, I. Y.; Lee, S. H.; Kim, D. W.; Yoon, S. M. Activated carbon nanocomposite electrodes for high performance supercapacitors. *Electrochim. Acta* **2013**, *102*, 240−245.

(18) Yuan, C. Z.; Li, J. Y.; Hou, L. R.; Zhang, X. G.; Shen, L. F.; Lou, X. W. Ultrathin mesoporous $NiCo_2O_4$ nanosheets supported on Ni foam as advanced electrodes for supercapacitors. *Adv. Funct. Mater.* **2012**, *22*, 4592−4597.

(19) Zhang, G. Q.; Lou, X. W. General solution growth of mesoporous $NiCo_2O_4$ nanosheets on various conductive substrates as high-performance electrodes for supercapacitors. *Adv. Mater.* **2013**, *25*, 976−979.

(20) Yang, P. F.; Song, B.; Wu, R.; Zheng, Y. F.; Sun, Y. F.; Jian, J. K. Solvothermal growth of NiS single-crystalline nanorod. *J. Alloys Compd.* **2009**, *481*, 450−454.

(21) Ni, Y. H.; Wang, X. X.; Hong, J. M. Fast reflux synthesis of multi-armed PbS dendrites, influencing factors and optical properties. *RSC Adv.* **2012**, *2*, 546−551.

(22) Wang, Y.; Herron, N. Nanometer-sized semiconductor clusters: Materials synthesis, quantum size effects, and photophysical propertles. *J. Phys. Chem.* **1991**, *95*, 525−532.

(23) Zhu, B. T.; Wang, Z. Y.; Ding, S. J.; Chen, J. S; Lou, X. W. Hierarchical nickel sulfide hollow spheres for high performance supercapacitors. *RSC Adv.* **2011**, *1*, 397−400.

(24) Zhang, L.; Zhou, L.; Wu, H. B; Xu, R.; Lou, X. W. Unusual formation of single-crystal manganese sulfide microboxes co-mediated by the cubic crystal structure and shape. *Angew. Chem., Int. Ed.* **2012**, *51*, 7267−7270.

(25) Li, G. P.; Zhai, J. F.; Li, D.; Fang, X. N.; Jiang, H.; Dong, Q. Z.; Wang, E. K. One-pot synthesis of monodispersed ZnS nanospheres with high antibacterial activity. *J. Mater. Chem.* **2010**, *20*, 9215−9219.

(26) Simmons, B.; Li, S. C.; John, V. T.; McPherson, G. L.; Taylor, C.; Schwartz, D. K.; Maskos, K. Spatial compartmentalization of nanoparticles into strands of a self-assembled organogel. *Nano Lett.* **2002**, *2*, 1037−1042.

(27) liang, W.; Whangbo, M. H. Conductivity anisotropy and structural phase transition in Covellite CuS. *Solid State Commun.* **1993**, *85*, 405−408.

(28) Wang, B.; Park, J. S.; Su, D. W.; Wang, C. Y.; Ahn, H. J.; Wang, G. X. Solvothermal synthesis of CoS_2−graphene nanocomposite material for high-performance supercapacitors. *J. Mater. Chem.* **2012**, *22*, 15750−15756.

(29) Yang, J. Q.; Duan, X. C.; Qin, Q.; Zhen, W. J. Solvothermal synthesis of hierarchicalflower-like β-NiS with excellent electrochemical performance for Supercapacitors. *J. Mater. Chem. A* **2013**, *1*, 7880−7884.

(30) Justin, P.; Rao, G. R. CoS spheres for high-rate electrochemical capacitive energy storage application. *Int. J. Hydrogen Energy* **2010**, *35*, 9709−9715.

(31) Zhang, L.; Wu, H. B.; Lou, X. W. Unusual CoS_2 ellipsoids with anisotropic tube-like cavities and their application in supercapacitors. *Chem. Commun.* **2012**, *48*, 6912−6914.

(32) Wan, H. Z.; Jiang, J. J.; Yu, J. W.; Xu, K.; Miao, L.; Zhang, L.; Chen, H. C.; Ruan, Y. J. $NiCo_2S_4$ porous nanotubes synthesisviasacrificial templates: high-performance electrode materials of supercapacitors. *CrystEngComm* **2013**, *51*, 7649−7651.

(33) Chen, H. C.; Jiang, J. J.; Zhang, L.; Wan, H. Z.; Qi, T.; Xia, D. D. Highly conductive $NiCo_2S_4$ urchin-like nanostructures for high-rate pseudocapacitors. *Nanoscale* **2013**, *5*, 8879−8883.

(34) Kirkendall, E. O. Diffusion of zinc in alpha brass. *Trans. AIME.* **1942**, *147*, 104−110.

(35) Wang, Z. H.; Pan, L.; Hu, H. B.; Zhao, S. P. Co_9S_8 nanotubes synthesized on the basis of nanoscale Kirkendall effect and their

magnetic and electrochemical properties. *CrystEngComm* **2010**, *12*, 1899−1904.
(36) Fan, H. J.; Gösele, U.; Zacharias, M. Formation of nanotubes and hollow nanoparticles based on kirkendall and diffusion processes: A review. *Small* **2007**, *3*, 1660−1671.
(37) Yin, Y.; Rioux, R. M.; Erdonmez, C. K.; Hughes, S.; Somorjai, G. A.; Alivisatos, A. P. Formation of hollow nanocrystals through the nanoscale Kirkendall Effect. *Science* **2004**, *304*, 711−714.
(38) Fan, H. J.; Knez, M.; Scholz, R.; Nielsch, K.; Pippel, E.; Hesse, D.; Zacharias, M.; Gössele, U. Monocrystalline spinel nanotube fabrication based on the Kirkendall effect. *Nat. Mater.* **2006**, *5*, 627−633.
(39) Chen, G. Z.; Sun, S. X.; Sun, X.; Fan, W. L.; You, T. Formation of CeO_2 nanotubes from $Ce(OH)CO_3$ nanorods through Kirkendall diffusion. *Inorg. Chem.* **2009**, *48*, 1334−1338.
(40) Liu, Q.; Jin, J. T.; Zhang, J. Y. $NiCo_2S_4$@graphene as a bifunctional electrocatalyst for oxygen reduction and evolution reactions. *ACS Appl. Mater. Interfaces* **2013**, *5*, 5002−5008.
(41) Wang, Q. H.; Jiao, L. F.; Du, H. M.; Si, Y. C.; Wang, Y. J.; Yuan, H. T. Co_3S_4 hollow nanospheres grown on graphene as advanced electrode materials for supercapacitors. *J. Mater. Chem.* **2012**, *22*, 21387−21391.
(42) Guan, C.; Xia, X. H.; Meng, N.; Zeng, Z. Y.; Cao, X. H.; Soci, C.; Zhang, H.; Fan, H. J. Hollow core−shell nanostructure supercapacitor electrodes: Gap matters. *Energy Environ. Sci.* **2012**, *5*, 9085−9090.
(43) Kim, K. S.; Park, S. J. Synthesis and high electrochemical capacitance of N-doped microporous carbon/carbon nanotubes for supercapacitor. *J. Electroanal. Chem.* **2012**, *673*, 58−64.
(44) Wang, W. S.; Dahl, M.; Yin, Y. D. Hollow nanocrystals through the nanoscale Kirkendall effect. *Chem. Mater.* **2013**, *25*, 1179−1189.
(45) Toupin, M.; Brousse, T.; Belanger, D. Influence of microstucture on the charge storage properties of chemically synthesized manganese dioxide. *Chem. Mater.* **2002**, *14*, 3946−3952.
(46) Bonso, J. S.; Rahy, A.; Perera, S. D.; Nourb, N.; Seitz, O.; Chabal, Y. J.; K. J., B., Jr; Ferraris, J. P.; Yang, D. J. Exfoliated graphite nanoplatelets−V_2O_5 nanotube composite electrodes for supercapacitors. *J. Power Sources* **2012**, *203*, 227−232.
(47) Tummala, R.; Guduru, R. K.; Mohanty, P. S. Nanostructured Co_3O_4 electrodes for supercapacitor applications from plasma spray technique. *J. Power Sources* **2012**, *209*, 44−51.
(48) Li, Z.; Zhang, L.; Amirkhiz, B. S.; Tan, X. H.; Xu, Z. W.; Wang, H. L.; Olsen, B. C.; Holt, C. M. B.; Mitlin, D. Carbonized chicken eggshell membranes with 3D architectures as high-performance electrode materials for supercapacitors. *Adv. Energy Mater.* **2012**, *2*, 431−437.
(49) Ma, Y.; Zhang, C.; Ji, G.; Lee, J. Y. Nitrogen-doped carbon-encapsulation of Fe_3O_4 for increased reversibility in Li^+ storage by the conversion reaction. *J. Mater. Chem.* **2012**, *22*, 7845−7850.